

Energy Spectrum of Ultrahigh-Energy Cosmic Rays across Declinations -90° to $+44.8^\circ$ as Measured at the Pierre Auger Observatory

A. Abdul Halim,¹ P. Abreu,² M. Aglietta,^{3,4} I. Allekotte,⁵ K. Almeida Cheminant,^{6,7} A. Almela,^{8,9} R. Aloisio,^{10,11} J. Alvarez-Muñiz,¹² A. Ambrosone,¹⁰ J. Ammerman Yebra,¹² G. A. Anastasi,^{13,14} L. Anchordoqui,¹⁵ B. Andrada,⁸ L. Andrade Dourado,^{10,11} S. Andringa,² L. Apollonio,^{16,17} C. Aramo,¹⁸ E. Arnone,^{19,4} J. C. Arteaga Velázquez,²⁰ P. Assis,² G. Avila,²¹ E. Avocone,^{22,11} A. Bakalova,²³ F. Barbato,^{10,11} A. Bartz Mocellin,²⁴ J. A. Bellido,¹ C. Berat,²⁵ M. E. Bertaina,^{19,4} M. Bianciotto,^{19,4} P. L. Biermann,²⁶ V. Binet,²⁷ K. Bismark,^{28,8} T. Bister,^{7,6} J. Biteau,^{29,30} J. Blazek,²³ J. Blümer,³¹ M. Boháčová,²³ D. Boncioli,^{22,11} C. Bonifazi,³² L. Bonneau Arbeletche,³³ N. Borodai,³⁴ J. Brack,³⁵ P. G. Brichetto Orchera,^{8,31} F. L. Briechele,³⁶ A. Bueno,³⁷ S. Buitink,³⁸ M. Buscemi,^{14,13} M. Büsken,^{28,8} A. Bwembya,^{7,6} K. S. Caballero-Mora,³⁹ S. Cabana-Freire,¹² L. Caccianiga,^{16,17} F. Campuzano,⁴⁰ J. Caraça-Valente,²⁴ R. Caruso,^{13,14} A. Castellina,^{3,4} F. Catalani,⁴¹ G. Cataldi,⁴² L. Cazon,¹² M. Cerda,⁴³ B. Čermáková,³¹ A. Cermenati,^{10,11} J. A. Chinellato,³³ J. Chudoba,²³ L. Chytka,⁴⁴ R. W. Clay,¹ A. C. Cobos Cerutti,⁴⁰ R. Colalillo,^{45,18} R. Conceição,² G. Consolati,^{17,46} M. Conte,^{47,42} F. Convenga,^{22,11} D. Correia dos Santos,⁴⁸ P. J. Costa,² C. E. Covault,⁴⁹ M. Cristinziani,⁵⁰ C. S. Cruz Sanchez,⁵¹ S. Dasso,^{52,53} K. Daumiller,³¹ B. R. Dawson,¹ R. M. de Almeida,⁴⁸ E.-T. de Boone,⁵⁰ B. de Errico,⁴⁸ J. de Jesús,^{8,31} S. J. de Jong,^{7,6} J. R. T. de Mello Neto,⁴⁸ I. De Mitri,^{10,11} J. de Oliveira,⁵⁴ D. de Oliveira Franco,⁵⁵ F. de Palma,^{47,42} V. de Souza,⁵⁶ E. De Vito,^{47,42} A. Del Popolo,^{13,14} O. Deligny,⁵⁷ N. Denner,²³ L. Deval,^{3,4} A. di Matteo,⁴ C. Dobrigkeit,³³ J. C. D'Olivo,⁵⁸ L. M. Domingues Mendes,^{59,2} Q. Dorosti,⁵⁰ J. C. dos Anjos,⁵⁹ R. C. dos Anjos,⁶⁰ J. Ebr,²³ F. Ellwanger,³¹ R. Engel,^{28,31} I. Epicoco,^{47,42} M. Erdmann,³⁶ A. Etchegoyen,^{8,9} C. Evoli,^{10,11} H. Falcke,^{7,6,16} G. Farrar,⁶² A. C. Fauth,³³ T. Fehler,⁵⁰ F. Feldbusch,⁶³ A. Fernandes,² M. Fernandez,⁶⁴ B. Fick,⁶⁵ J. M. Figueira,⁸ P. Filip,^{28,8} A. Filipčič,^{66,67} T. Fitoussi,³¹ B. Flaggs,⁶⁸ T. Fodran,⁷ A. Franco,⁴² M. Freitas,² T. Fujii,^{69,*} A. Fuster,^{8,9} C. Galea,⁷ B. García,⁴⁰ C. Gaudu,⁷⁰ P. L. Ghia,⁵⁷ U. Giaccari,⁴² F. Gobbi,⁴³ F. Gollan,⁸ G. Golup,⁵ M. Gómez Berisso,⁵ P. F. Gómez Vitale,²¹ J. P. Gongora,²¹ J. M. González,⁵ N. González,⁸ D. Góra,³⁴ A. Gorgi,^{3,4} M. Gottowik,³¹ F. Guarino,^{45,18} G. P. Guedes,⁷¹ E. Guido,⁵⁰ L. Güllow,³¹ S. Hahn,²⁸ P. Hamal,²³ M. R. Hampel,⁸ P. Hansen,⁵¹ V. M. Harvey,¹ A. Haungs,³¹ T. Hebbeker,³⁶ C. Hojvat,⁷² J. R. Hörandel,^{7,6} P. Horvath,⁴⁴ M. Hrabovský,⁴⁴ T. Huege,^{31,38} A. Insolia,^{13,14} P. G. Isar,⁷³ M. Ismaiel,^{7,6} P. Janecek,²³ V. Jilek,²³ K.-H. Kampert,⁷⁰ B. Keilhauer,³¹ A. Khakurdikar,⁷ V. V. Kizakke Covilakam,^{8,31} H. O. Klages,³¹ M. Kleifges,⁶³ J. Köhler,³¹ F. Krieger,³⁶ M. Kubatova,²³ N. Kunka,⁶³ B. L. Lago,⁷⁴ N. Langner,³⁶ N. Leal,⁸ M. A. Leigui de Oliveira,⁷⁵ Y. Lema-Capeans,¹² A. Letessier-Selvon,⁷⁶ I. Lhenry-Yvon,⁵⁷ L. Lopes,² J. P. Lundquist,⁶⁷ M. Mallamaci,^{77,14} D. Mandat,²³ P. Mantsch,⁷² F. M. Mariani,^{16,17} A. G. Mariazzi,⁵¹ I. C. Mariş,⁶⁴ G. Marsella,^{77,14} D. Martello,^{47,42} S. Martinelli,^{31,8} M. A. Martins,¹² H.-J. Mathes,³¹ J. Matthews,⁷⁸ G. Matthiae,^{79,80} E. Mayotte,²⁴ S. Mayotte,²⁴ P. O. Mazur,⁷² G. Medina-Tanco,⁵⁸ J. Meinert,⁷⁰ D. Melo,⁸ A. Menshikov,⁶³ C. Merx,³¹ S. Michal,²³ M. I. Micheletti,²⁷ L. Miramonti,^{16,17} M. Mogarkar,³⁴ S. Mollerach,⁵ F. Montanet,²⁵ L. Morejon,⁷⁰ K. Mulrey,^{7,6} R. Mussa,⁴ W. M. Namasaka,⁷⁰ S. Negi,²³ L. Nellen,⁵⁸ K. Nguyen,⁶⁵ G. Nicora,⁸¹ M. Niechciol,⁵⁰ D. Nitz,⁶⁵ D. Nosek,⁸² A. Novikov,⁶⁸ V. Novotny,⁸² L. Nožka,⁴⁴ A. Nucita,^{47,42} L. A. Núñez,⁸³ J. Ochoa,^{8,31} C. Oliveira,⁵⁶ L. Östman,²³ M. Palatka,²³ J. Pallotta,⁸¹ S. Panja,²³ G. Parente,¹² T. Paulsen,⁷⁰ J. Pawlowsky,⁷⁰ M. Pech,²³ J. Pękała,³⁴ R. Pelayo,⁸⁴ V. Pelgrims,⁶⁴ L. A. S. Pereira,⁸⁵ E. E. Pereira Martins,^{28,8} C. Pérez Bertolli,^{8,31} L. Perrone,^{47,42} S. Petrera,^{10,11} C. Petrucci,²² T. Pierog,³¹ M. Pimenta,² M. Platino,⁸ B. Pont,⁷ M. Pourmohammad Shahvar,^{77,14} P. Privitera,⁶⁹ C. Priyadarshi,³⁴ M. Prouza,²³ K. Pytel,⁸⁶ S. Querschfeld,⁷⁰ J. Rautenberg,⁷⁰ D. Ravignani,⁸ J. V. Reginatto Akim,³³ A. Reuzki,³⁶ J. Ridky,²³ F. Riehn,^{12,†} M. Risse,⁵⁰ V. Rizi,^{22,11} E. Rodriguez,^{8,31} G. Rodriguez Fernandez,⁸⁰ J. Rodriguez Rojo,²¹ S. Rossoni,⁵⁵ M. Roth,³¹ E. Roulet,⁵ A. C. Rovero,⁵² A. Saftoiu,⁸⁷ M. Saharan,⁷ F. Salamida,^{22,11} H. Salazar,⁸⁸ G. Salina,⁸⁰ P. Sampathkumar,³¹ N. San Martin,²⁴ J. D. Sanabria Gomez,⁸³ F. Sánchez,⁸ E. M. Santos,⁸⁹ E. Santos,²³ F. Sarazin,²⁴ R. Sarmento,² R. Sato,²¹ P. Savina,^{10,11} V. Scherini,^{47,42} H. Schieler,³¹ M. Schimassek,⁵⁷ M. Schimp,⁷⁰ D. Schmidt,³¹ O. Scholten,^{38,‡} H. Schoorlemmer,^{7,6} P. Schovánek,²³ F. G. Schröder,^{68,31} J. Schulte,³⁶ T. Schulz,²³ S. J. Sciutto,⁵¹ M. Scornavacche,^{8,31} A. Sedoski,⁸ A. Segreto,^{90,14} S. Sehgal,⁷⁰ S. U. Shivashankara,⁶⁷ G. Sigl,⁵⁵ K. Simkova,^{38,64}

F. Simon,⁶³ R. Šmída,⁶⁹ P. Sommers,⁹¹ R. Squartini,⁴³ M. Stadelmaier,^{31,17,16} S. Stanič,⁶⁷ J. Stasielak,³⁴ P. Stassi,²⁵ S. Strähnz,²⁸ M. Straub,³⁶ T. Suomijärvi,²⁹ A. D. Supanitsky,⁸ Z. Svozilikova,²³ K. Syrokvass,⁸² Z. Szadkowski,⁸⁶ F. Tairli,¹ M. Tambone,^{45,18} A. Tapia,⁹² C. Taricco,^{19,4} C. Timmermans,^{6,7} O. Tkachenko,²³ P. Tobiska,²³ C. J. Todero Peixoto,⁴¹ B. Tomé,² A. Travaini,⁴³ P. Travnicek,²³ M. Tueros,⁵¹ M. Unger,³¹ R. Uzeiroska,⁷⁰ L. Vaclavek,⁴⁴ M. Vacula,⁴⁴ I. Vaiman,^{10,11} J. F. Valdés Galicia,⁵⁸ L. Valore,^{45,18} P. van Dillen,^{7,6} E. Varela,⁸⁸ V. Vašíčková,⁷⁰ A. Vásquez-Ramírez,⁸³ D. Veberič,³¹ I. D. Vergara Quispe,⁵¹ S. Verpoest,⁶⁸ V. Verzi,⁸⁰ J. Vicha,²³ J. Vink,⁹³ S. Vorobiov,⁶⁷ J. B. Vuta,²³ C. Watanabe,⁴⁸ A. A. Watson,⁹⁴ A. Weindl,³¹ M. Weitz,⁷⁰ L. Wiencke,²⁴ H. Wilczyński,³⁴ B. Wundheiler,⁸ B. Yue,⁷⁰ A. Yushkov,²³ E. Zas,¹² D. Zavrtanik,^{67,66} and M. Zavrtanik^{66,67}

(Pierre Auger Collaboration)[§]

¹University of Adelaide, Adelaide, South Australia, Australia

²Laboratório de Instrumentação e Física Experimental de Partículas—LIP and Instituto Superior Técnico—IST, Universidade de Lisboa—UL, Lisboa, Portugal

³Osservatorio Astrofisico di Torino (INAF), Torino, Italy

⁴INFN, Sezione di Torino, Torino, Italy

⁵Centro Atómico Bariloche and Instituto Balseiro (CNEA-UNCuyo-CONICET), San Carlos de Bariloche, Argentina

⁶Nationaal Instituut voor Kernfysica en Hoge Energie Fysica (NIKHEF), Science Park, Amsterdam, The Netherlands

⁷IMAPP, Radboud University Nijmegen, Nijmegen, The Netherlands

⁸Instituto de Tecnologías en Detección y Astroparticulas (CNEA, CONICET, UNSAM), Buenos Aires, Argentina

⁹Universidad Tecnológica Nacional—Facultad Regional Buenos Aires, Buenos Aires, Argentina

¹⁰Gran Sasso Science Institute, L'Aquila, Italy

¹¹INFN Laboratori Nazionali del Gran Sasso, Assergi (L'Aquila), Italy

¹²Instituto Galego de Física de Altas Enerxías (IGFAE), Universidade de Santiago de Compostela, Santiago de Compostela, Spain

¹³Università di Catania, Dipartimento di Fisica e Astronomia “Ettore Majorana,” Catania, Italy

¹⁴INFN, Sezione di Catania, Catania, Italy

¹⁵Department of Physics and Astronomy, Lehman College, City University of New York, Bronx, NY, USA

¹⁶Università di Milano, Dipartimento di Fisica, Milano, Italy

¹⁷INFN, Sezione di Milano, Milano, Italy

¹⁸INFN, Sezione di Napoli, Napoli, Italy

¹⁹Università Torino, Dipartimento di Fisica, Torino, Italy

²⁰Universidad Michoacana de San Nicolás de Hidalgo, Morelia, Michoacán, México

²¹Observatorio Pierre Auger and Comisión Nacional de Energía Atómica, Malargüe, Argentina

²²Università dell'Aquila, Dipartimento di Scienze Fisiche e Chimiche, L'Aquila, Italy

²³Institute of Physics of the Czech Academy of Sciences, Prague, Czech Republic

²⁴Colorado School of Mines, Golden, Colorado, USA

²⁵Université Grenoble Alpes, CNRS, Grenoble Institute of Engineering Université Grenoble Alpes, LPSC-IN2P3, 38000 Grenoble, France

²⁶Max-Planck-Institut für Radioastronomie, Bonn, Germany

²⁷Instituto de Física de Rosario (IFIR)—CONICET/U.N.R. and Facultad de Ciencias Bioquímicas y Farmacéuticas U.N.R., Rosario, Argentina

²⁸Karlsruhe Institute of Technology (KIT), Institute for Experimental Particle Physics, Karlsruhe, Germany

²⁹Université Paris-Saclay, CNRS/IN2P3, IJCLab, Orsay, France

³⁰Institut universitaire de France (IUF), Paris, France

³¹Karlsruhe Institute of Technology (KIT), Institute for Astroparticle Physics, Karlsruhe, Germany

³²International Center of Advanced Studies and Instituto de Ciencias Físicas, ECyT-UNSAM and CONICET, Campus Miguelete—San Martín, Buenos Aires, Argentina

³³Universidade Estadual de Campinas (UNICAMP), IFGW, Campinas, SP, Brazil

³⁴Institute of Nuclear Physics PAN, Krakow, Poland

³⁵Colorado State University, Fort Collins, Colorado, USA

³⁶RWTH Aachen University, III. Physikalisches Institut A, Aachen, Germany

³⁷Universidad de Granada and C.A.F.P.E., Granada, Spain

³⁸Vrije Universiteit Brussels, Brussels, Belgium

- ³⁹Universidad Autónoma de Chiapas, Tuxtla Gutiérrez, Chiapas, México
- ⁴⁰Instituto de Tecnologías en Detección y Astropartículas (CNEA, CONICET, UNSAM),
and Universidad Tecnológica Nacional—Facultad Regional Mendoza (CONICET/CNEA), Mendoza, Argentina
- ⁴¹Universidade de São Paulo, Escola de Engenharia de Lorena, Lorena, São Paulo, Brazil
- ⁴²INFN, Sezione di Lecce, Lecce, Italy
- ⁴³Observatorio Pierre Auger, Malargüe, Argentina
- ⁴⁴Palacky University, Olomouc, Czech Republic
- ⁴⁵Università di Napoli “Federico II,” Dipartimento di Fisica “Ettore Pancini,” Napoli, Italy
- ⁴⁶Politecnico di Milano, Dipartimento di Scienze e Tecnologie Aerospaziali, Milano, Italy
- ⁴⁷Università del Salento, Dipartimento di Matematica e Fisica “E. De Giorgi,” Lecce, Italy
- ⁴⁸Universidade Federal do Rio de Janeiro, Instituto de Física, Rio de Janeiro, Rio de Janeiro, Brazil
- ⁴⁹Case Western Reserve University, Cleveland, Ohio, USA
- ⁵⁰Universität Siegen, Department Physik—Experimentelle Teilchenphysik, Siegen, Germany
- ⁵¹IFLP, Universidad Nacional de La Plata and CONICET, La Plata, Argentina
- ⁵²Instituto de Astronomía y Física del Espacio (IAFE, CONICET-UBA), Buenos Aires, Argentina
- ⁵³Departamento de Física and Departamento de Ciencias de la Atmósfera y los Océanos, FCEyN,
Universidad de Buenos Aires and CONICET, Buenos Aires, Argentina
- ⁵⁴Instituto Federal de Educação, Ciência e Tecnologia do Rio de Janeiro (IFRJ), Rio de Janeiro, Brazil
- ⁵⁵Universität Hamburg, II. Institut für Theoretische Physik, Hamburg, Germany
- ⁵⁶Universidade de São Paulo, Instituto de Física de São Carlos, São Carlos, São Paulo, Brazil
- ⁵⁷CNRS/IN2P3, IJCLab, Université Paris-Saclay, Orsay, France
- ⁵⁸Universidad Autónoma de México, México, DF, México
- ⁵⁹Centro Brasileiro de Pesquisas Físicas, Rio de Janeiro, Rio de Janeiro, Brazil
- ⁶⁰Universidade Federal do Paraná, Setor Palotina, Palotina, Brazil
- ⁶¹Stichting Astronomisch Onderzoek in Nederland (ASTRON), Dwingeloo, The Netherlands
- ⁶²New York University, New York, New York, USA
- ⁶³Karlsruhe Institute of Technology (KIT), Institut für Prozessdatenverarbeitung und Elektronik, Karlsruhe, Germany
- ⁶⁴Université Libre de Bruxelles (ULB), Brussels, Belgium
- ⁶⁵Michigan Technological University, Houghton, Michigan, USA
- ⁶⁶Experimental Particle Physics Department, Jožef Stefan Institute, Ljubljana, Slovenia
- ⁶⁷Center for Astrophysics and Cosmology (CAC), University of Nova Gorica, Nova Gorica, Slovenia
- ⁶⁸University of Delaware, Department of Physics and Astronomy, Bartol Research Institute, Newark, Delaware, USA
- ⁶⁹University of Chicago, Enrico Fermi Institute, Chicago, Illinois, USA
- ⁷⁰Bergische Universität Wuppertal, Department of Physics, Wuppertal, Germany
- ⁷¹Universidade Estadual de Feira de Santana, Feira de Santana, Brazil
- ⁷²Fermi National Accelerator Laboratory, Fermilab, Batavia, Illinois, USA
- ⁷³Institute of Space Science, Bucharest-Magurele, Romania
- ⁷⁴Centro Federal de Educação Tecnológica Celso Suckow da Fonseca, Petropolis, Brazil
- ⁷⁵Universidade Federal do ABC, Santo André, São Paulo, Brazil
- ⁷⁶Laboratoire de Physique Nucléaire et de Hautes Energies (LPNHE), Sorbonne Université, Université de Paris,
CNRS-IN2P3, Paris, France
- ⁷⁷Università di Palermo, Dipartimento di Fisica e Chimica “E. Segrè,” Palermo, Italy
- ⁷⁸Louisiana State University, Baton Rouge, Louisiana, USA
- ⁷⁹Università di Roma “Tor Vergata,” Dipartimento di Fisica, Roma, Italy
- ⁸⁰INFN, Sezione di Roma “Tor Vergata,” Roma, Italy
- ⁸¹Laboratorio Atmósfera—Departamento de Investigaciones en Láseres y sus Aplicaciones—UNIDEF (CITEDEF-CONICET),
Buenos Aires, Argentina
- ⁸²Charles University, Faculty of Mathematics and Physics, Institute of Particle and Nuclear Physics,
Prague, Czech Republic
- ⁸³Universidad Industrial de Santander, Bucaramanga, Colombia
- ⁸⁴Unidad Profesional Interdisciplinaria en Ingeniería y Tecnologías Avanzadas del Instituto Politécnico Nacional (UPIITA-IPN),
México, DF, México
- ⁸⁵Universidade Federal de Campina Grande, Centro de Ciências e Tecnologia,
Campina Grande, Brazil
- ⁸⁶University of Łódź, Faculty of High-Energy Astrophysics, Łódź, Poland
- ⁸⁷“Horia Hulubei” National Institute for Physics and Nuclear Engineering, Bucharest-Magurele, Romania
- ⁸⁸Benemérita Universidad Autónoma de Puebla, Puebla, México
- ⁸⁹Universidade de São Paulo, Instituto de Física, São Paulo, São Paulo, Brazil
- ⁹⁰Istituto di Astrofisica Spaziale e Fisica Cosmica di Palermo (INAF), Palermo, Italy
- ⁹¹Pennsylvania State University, University Park, Pennsylvania, USA

⁹²*Universidad de Medellín, Medellín, Colombia*⁹³*Universiteit van Amsterdam, Faculty of Science, Amsterdam, The Netherlands*⁹⁴*School of Physics and Astronomy, University of Leeds, Leeds, United Kingdom*

(Received 16 June 2025; accepted 22 October 2025; published 9 December 2025)

The energy spectrum of cosmic rays above 2.5 EeV has been measured across the declination range $-90^\circ \leq \delta \leq +44.8^\circ$ using $\sim 310\,000$ events accrued at the Pierre Auger Observatory from an exposure of $(104\,900 \pm 3\,100)$ km² sr yr. No significant variations of energy spectra with declination are observed, after allowing or not for nonuniformities across the sky arising from the well-established dipolar anisotropies in the arrival directions of ultrahigh-energy cosmic rays. The instep feature in the spectrum at $\simeq 10$ EeV reported previously is now established at a significance above 5σ . Within the statistics, the energy spectra are indistinguishable across declinations so disfavoring an origin for the instep from a few distinctive sources.

DOI: [10.1103/p415-hxlf](https://doi.org/10.1103/p415-hxlf)

Introduction—The discovery at the Pierre Auger Observatory [1] of a dipole in the distribution of cosmic rays of energy above 8 EeV of amplitude $\sim 6\%$ at a significance of over 5σ marks a significant advance in the field of high-energy cosmic-ray astronomy [2]. The status of this result is now 6.8σ , with an increase of the dipole amplitude with energy identified [3]. Above 32 EeV, associations of high-energy cosmic rays with an overdensity in the Centaurus region, and with starburst galaxies, have been found, but only at the 4σ level [4]. Beyond 100 EeV, the arrival direction distribution across the whole sky, derived from a combination of data from the Auger Observatory and the Telescope Array, is featureless [5]. It is thus important to examine whether the energy spectrum varies with declination, particularly at the highest energies, where the new spectral feature near 10 EeV, identified in data from the Auger Observatory [6], indicates a two-step suppression of the spectrum [7,8]. An analysis of spectra in bands of declination is presented, exploiting the 1.2 m deep-water Cherenkov detectors of the Auger Observatory to obtain measurements over declinations -90° to $+44.8^\circ$.

At large zenith angles θ , the effects of the geomagnetic field on the distribution of the muons in air showers increases so that the near-circular symmetry of signals around the shower axis found at low zenith angles is destroyed: above 70° , eccentricities over 0.9 are found. Accordingly, different methods of analysis are necessary for “vertical showers” ($\theta \leq 60^\circ$) and for the more “inclined events” (60° – 80°). The procedures for dealing with events with $\theta \leq 60^\circ$ are classical [9,10]. Techniques to reconstruct

events where the geomagnetic field is important were developed more recently [11], with the methods later adapted for use with data from the Auger Observatory. The procedure to obtain the energy of the primary particle for vertical showers is based on the determination of the signal in the water-Cherenkov detectors, $S(1000)$, interpolated at 1000 m from the center of the shower [12], while for inclined events a parameter based on the number of muons in the shower, N_{19} , has been adopted [13,14]. $S(1000)$ and N_{19} are subsequently converted into size parameters S_{38} and N_{68} , independent of the zenith angle, using the constant intensity method [6,15]. Calorimetric estimates of primary energies are derived by calibrating these size parameters using fluorescence measurements, obtained on clear, moonless nights. Derivation of the energy spectrum from vertical events requires no assumptions about features of hadronic interactions at high energies or of the mass of the primary cosmic rays, apart from a 1.5% systematic uncertainty in the estimation of the invisible energy [6,16]. Minimal assumptions about these parameters are required for the inclined events [17,18]. Data used here were recorded between January 1, 2004, and December 31, 2022. For vertical events the exposure was $\mathcal{E}_{[0-60^\circ]} = (81, 100 \pm 2400)$ km² sr yr, with 279,131 events recorded above 2.5 EeV, while for inclined showers 31,543 events above 4 EeV were recorded in an exposure of $\mathcal{E}_{[60-80^\circ]} = (23, 800 \pm 700)$ km² sr yr. Exposures are independent of energy above these thresholds [6,17], which are nonidentical mainly due to the attenuation of the electromagnetic cascade at high zenith angles.

Combination of individual spectra—Given the latitude of the Observatory, $\lambda \simeq -35.2^\circ$ and the zenith angle ranges mentioned in the previous section, the S_{38} -based dataset covers the range of declinations $-90^\circ \leq \delta \leq +24.8^\circ$ in equatorial coordinates, whereas the N_{68} one covers $-84.8^\circ \leq \delta \leq +44.8^\circ$. Our aim is to measure the spectrum over the whole declination range covered with the surface array, $-90^\circ \leq \delta \leq +44.8^\circ$. Thus the independent spectra

*Present address: Graduate School of Science, Osaka Metropolitan University, Osaka, Japan.

†Present address: Technische Universität Dortmund and Ruhr-Universität Bochum, Dortmund and Bochum, Germany.

‡Also at Kapteyn Institute, University of Groningen, Groningen, The Netherlands.

§Contact author: spokespersons@auger.org;
<http://www.auger.org>

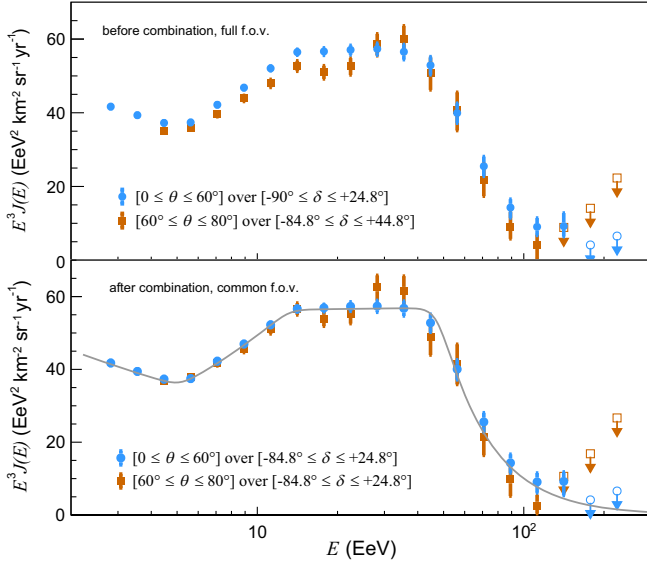


FIG. 1. Individual energy spectra scaled by E^3 inferred from S_{38} - and N_{68} -based analyses before (top panel) and after (bottom panel) correcting the energies of inclined events to a best-fit common energy scale. The declination range after combination is reduced to $[-84.8^\circ, +24.8^\circ]$ to guarantee observation of the same sky. Upper limits at 90% confidence level are shown in empty bins. The grey line is the best fit to data points after combination.

from the S_{38} - and N_{68} -based analyses, shown as the circles and squares, respectively, in the top panel of Fig. 1, must be combined.

The combination procedure follows from that in [19]. The combined spectrum is obtained by forward-folding the effects of the finite energy accuracy of the detector into a proposed function tailored to describe a series of power-law falloffs,

$$J(E; \mathbf{p}) = J_0 \left(\frac{E}{E_0} \right)^{-\gamma_0} \frac{\prod_{j=1}^3 \left[1 + \left(\frac{E}{E_{jk}} \right)^{\omega_{jk}^{-1}} \right]^{(\gamma_j - \gamma_k) \omega_{jk}}}{\prod_{j=1}^3 \left[1 + \left(\frac{E_0}{E_{jk}} \right)^{\omega_{jk}^{-1}} \right]^{(\gamma_j - \gamma_k) \omega_{jk}}}, \quad (1)$$

with $k = j + 1$ and eight free parameters encompassed in \mathbf{p} , namely the overall normalization J_0 , four spectral indices $(\gamma_0, \gamma_1, \gamma_2, \gamma_3)$, and three energy turning points E_{jk} ; the parameters ω_{jk} that govern the width of the transition from γ_j to γ_k are fixed to $\omega_{jk} = 0.05$ [6]; the pivot energy is chosen as $E_0 = 10^{0.5}$ EeV. The parameters \mathbf{p} are adjusted to obtain the best match between the observed number of events n_i in each differential energy bin of width $\Delta \log_{10} E = 0.1$ and the expected ones $\nu_i(\mathbf{p})$ simultaneously for both data streams. The minimization procedure is based on the product of Poissonian likelihood functions pertaining to each individual spectrum, $\mathcal{L}_{[0-60^\circ]}$ and $\mathcal{L}_{[60^\circ-80^\circ]}$.

Both individual spectra are subject to systematic uncertainties, with contributions from the absolute energy scale

(14%) [20], the exposure (3%) [21], the unfolding procedure ($\leq 2\%$) [6], and the energies inferred from S_{38} and N_{68} ($\leq 3\%$) [6,14]. No indication of further systematics has been found from a comparison of spectra calculated over different time periods, seasons, and ranges of zenith angle.

The systematic uncertainties relating to each S_{38} - and N_{68} -based analysis are common to both: the important exception concerns those inherited from the energy-calibration procedure that are uncorrelated as the two datasets used for calibration are independent. The largest uncertainties are related to the calibration of N_{68} , as it is based on 605 events compared to 4703 for S_{38} . The statistics is limited by the high-quality criteria used to guarantee an accurate energy estimation with the fluorescence technique, and by the effective area for observing the maximum of shower development that drops rapidly with zenith angle [22,23]. Therefore, our strategy for the combination is to correct the energies of the N_{68} -based dataset, originally determined as $E = AN_{68}^B$, to a best-fit common energy scale, using two absolute departure parameters δA and δB such that $E' = (A + \delta A)N_{68}^{B+\delta B}$. As shown below, considering the uncertainties in N_{68} alone, the most significant ones will suffice to obtain a satisfactory goodness of fit. Including those in S_{38} would improve further the combination, but is unnecessary.

In addition, as explained in the Appendix A, the energy calibration of N_{68} may be affected by (logarithmic) nonlinearities above ~ 10 EeV due to the sensitivity of N_{68} to the small, yet sharp, changes in mass composition recently uncovered [24,25] and to experimental effects. A third departure parameter, δC , is therefore introduced so that the correction reads $E'' = (A + \delta A)N_{68}^{B+\delta B+\delta C}$ above 10 EeV.

During each step of the fit, the energy-bin boundaries of the N_{68} -based analysis are corrected by varying the extra parameters $\mathbf{x} = (\delta A, \delta B, \delta C)$ that govern the uncorrelated systematic uncertainties. Correspondingly, an extra term in the joint likelihood restricts the values of the extra parameters within their uncertainties. It is constructed by considering on the one hand the sum of two random variables δB and δC , and on the other hand the correlation between δA and δB . The log-likelihood function therefore stems from the convolution of a 2D Gaussian with correlation parameter $\rho \simeq -0.66$ with a 1D Gaussian pertaining to δC alone,

$$-2 \ln \mathcal{L}_{\mathbf{x}}(\delta A, \delta B, \delta C) = \frac{\delta A^2 (\sigma_B^2 + \sigma_C^2) - 2\rho \delta A \delta B \sigma_A \sigma_B + (\delta B + \delta C)^2 \sigma_A^2}{\sigma_A^2 (\sigma_C^2 + \sigma_B^2 (1 - \rho^2))}, \quad (2)$$

with $\sigma_A \simeq 6 \times 10^{-2}$ EeV, $\sigma_B = 1.4 \times 10^{-2}$ and, as shown in the Appendix A, $\sigma_C = 3 \times 10^{-2}$ from the systematic uncertainties in N_{68} and in the relationship between N_{68} and energy.

In this way, for unrealistic changes in $(\delta A, \delta B, \delta C)$, the $-2 \ln \mathcal{L}_{\mathbf{x}}(\delta A, \delta B, \delta C)$ term acts as a penalty factor while minimizing the total log-likelihood function $-2 \ln \mathcal{L}(\mathbf{p}, \mathbf{x})$, which, overall, reads as

$$\mathcal{L}(\mathbf{p}, \mathbf{x}) = \mathcal{L}_{[0-60^\circ]}(\mathbf{p}, \mathbf{x}) \times \mathcal{L}_{[60^\circ-80^\circ]}(\mathbf{p}, \mathbf{x}) \times \mathcal{L}_{\mathbf{x}}(\mathbf{x}). \quad (3)$$

The outcome of the forward folding is the set of parameters \mathbf{p} , and \mathbf{x} , that allows calculation of ν_i and μ_i , which are the expected number of events including and not including the detector effects, respectively. Unfolding factors, defined as $c_i = \mu_i/\nu_i$, are then applied to correct for bin-to-bin migration induced by the finite accuracy of the response functions, which are determined in a data-driven manner [6] and given in the Appendix A. The resulting spectral point for each bin is obtained as

$$J_i = \frac{c_i n_{i[0-60^\circ]} + c_i n_{i[60^\circ-80^\circ]}}{\mathcal{E}_i \Delta E_i}, \quad (4)$$

with $\mathcal{E}_i = \mathcal{E}_{[0-60^\circ]}$ for $0.4 \leq \log_{10}(E/\text{EeV}) \leq 0.6$ and $\mathcal{E}_i = \mathcal{E}_{[0-60^\circ]} + \mathcal{E}_{[60^\circ-80^\circ]}$ for $\log_{10}(E/\text{EeV}) \geq 0.6$. The minimization procedure, applied only to the events in the declination band $[-84.8^\circ, +24.8^\circ]$, common to both datasets, to guarantee observation of the same sky so that spectra must be in statistical agreement, yields values of $\delta A/A \simeq (3.0 \pm 0.6)\%$, $\delta B/B \simeq (0.3 \pm 1.5)\%$, respectively corresponding to shifts of $2.6\sigma_A$ and $0.2\sigma_B$, and $\delta C \simeq (-2.0 \pm 2.0) \times 10^{-2}$. The resulting spectra are displayed in the lower panel of Fig. 1. The most significant changes are in the lower energy bins, where the statistical power is greatest. Note that, as the analysis is designed so that $\mathcal{L}_{[0-60^\circ]}(\mathbf{p}, \mathbf{x})$ is independent of \mathbf{x} , the changes impact dominantly the N_{68} -based spectrum. The combined spectrum obtained with Eq. (4) shows a deviance of $D = 40.5$, which, if considered to follow a ‘‘C statistics’’ [26], can be compared to the expectation of $\langle D \rangle = 26.9 \pm 7.0$ to yield a p -value of $\simeq 0.12$.

Searches for declination dependences—The best-fit parameters for $(\delta A, \delta B, \delta C)$ that yield statistical agreement of spectra in the declination range $[-84.8^\circ, +24.8^\circ]$ are used to search for declination dependences in five ranges over $[-90^\circ, +44.8^\circ]$. The first range corresponds to the most northerly declination band $[+24.8^\circ, +44.8^\circ]$: it is selected

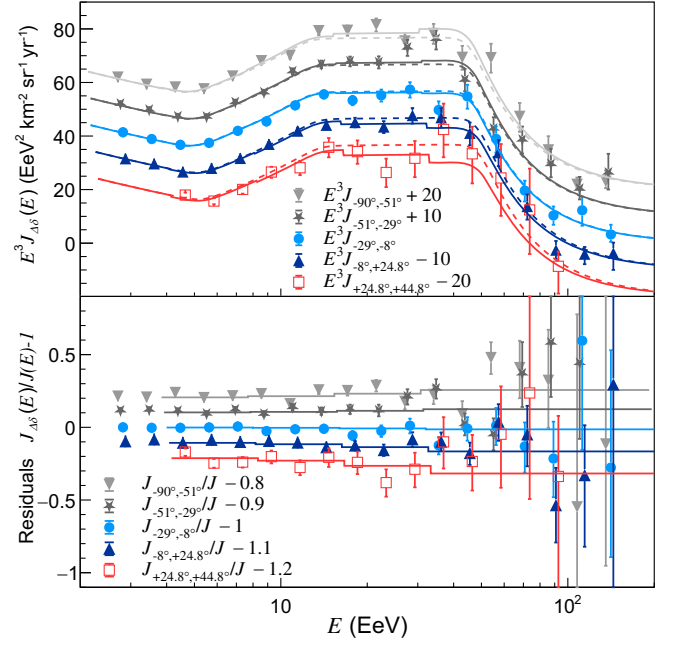


FIG. 2. Top: energy spectra in five declination ranges. The dotted reference lines are the best-fit function for the spectrum combined over $[-84.8^\circ, +24.8^\circ]$; the full lines account for the impact of dipole anisotropies in each band. Bottom: corresponding residuals. Artificial shifts are applied for visualization purpose. An alternative view of the residuals is provided in the Appendix A. Data are available in the Appendix B.

as it only contains inclined events (5632 after energy corrections for an exposure of $(4100 \pm 120) \text{ km}^2 \text{ sr yr}$) and it is thus not considered in the combination fit. The remaining portion of the sky $[-90^\circ, +24.8^\circ]$ is divided in four declination ranges with exposures similar to within 1% and averaging $25,000 \text{ km}^2 \text{ sr yr}$. Detailed comparisons of the spectra in the five declination bands are shown in Fig. 2. In the top panel, individual spectra are compared with the best-fit function (dotted lines) for the spectrum combined over $[-84.8^\circ, +24.8^\circ]$ and with the same best-fit function (full lines) taking into account the variation of the dipole amplitude with energy and declination measured above 4 EeV. Because the energy-spectrum estimator is based primarily on the observed number of events through the directional exposure function $\omega(\delta)$, the expression of $J_{\Delta\delta}(E; \mathbf{p})$ is obtained as [6],

$$J_{\Delta\delta}(E; \mathbf{p}) = J(E; \mathbf{p}) \left(1 + \frac{\mathcal{E}_0 \int_{\Delta\delta} d\delta \cos \delta \omega(\delta) + d_z(E) \int_{\Delta\delta} d\delta \cos \delta \sin \delta \omega(\delta)}{\mathcal{E}_{\Delta\delta} \int d\delta \cos \delta \omega(\delta) + d_z(E) \int d\delta \cos \delta \sin \delta \omega(\delta)} \right), \quad (5)$$

with \mathcal{E}_0 the total exposure over the declination range of reference $[-84.8^\circ, +24.8^\circ]$, $\mathcal{E}_{\Delta\delta}$ that over the declination band under consideration, and where the integrations in the denominator are carried out over $[-84.8^\circ, +24.8^\circ]$. The coefficients $d_z(E)$ read $\{-0.013, -0.031, -0.070\}$ in

differential bins of width $\Delta \log_{10} E = 0.3$ between 4 and 32 EeV and -0.13 above 32 EeV [3]. In the bottom panel, the best-fit function over $[-84.8^\circ, +24.8^\circ]$ is taken as a reference and the residual differences from this spectrum are compared with expectations. The residuals follow the

TABLE I. Spectral parameters \mathbf{p} in several declination bands: normalization J_0 in $\text{km}^{-2} \text{sr}^{-1} \text{yr}^{-1} \text{EeV}^{-1}$ units, indices γ_j and break energies E_{jk} in EeV units; and probabilities $P(\geq Q^2)$ that $\mathbf{p}_{\Delta\delta}$ departs from \mathbf{p}_{ref} measured across $[-84.8^\circ, +24.8^\circ]$. In the declination band $[+24.8^\circ, +44.8^\circ]$, the threshold of the N_{68} -based analysis does not allow for measuring γ_1 and E_{12} , which are fixed to their value found across $[-84.8^\circ, +24.8^\circ]$.

$[\delta_{\text{min}}, \delta_{\text{max}}]$	J_0	γ_1	γ_2	γ_3	γ_4	E_{12}	E_{23}	E_{34}	$P(\geq Q^2)$ (%)
$[-84.8^\circ, +24.8^\circ]$	1.271 ± 0.004	3.26 ± 0.01	2.51 ± 0.03	2.99 ± 0.03	5.3 ± 0.2	5.1 ± 0.1	13 ± 1	48 ± 2	...
$[-90^\circ, -51^\circ]$	1.278 ± 0.007	3.24 ± 0.02	2.54 ± 0.06	3.18 ± 0.06	7.2 ± 1.0	5.1 ± 0.2	17 ± 2	62 ± 4	23
$[-51^\circ, -29^\circ]$	1.281 ± 0.007	3.26 ± 0.02	2.46 ± 0.06	2.87 ± 0.06	4.6 ± 0.4	5.2 ± 0.2	12 ± 2	39 ± 4	13
$[-29^\circ, -8^\circ]$	1.257 ± 0.007	3.28 ± 0.02	2.54 ± 0.06	3.02 ± 0.06	5.6 ± 0.4	4.9 ± 0.2	13 ± 2	49 ± 4	71
$[-8^\circ, +24.8^\circ]$	1.266 ± 0.007	3.26 ± 0.02	2.50 ± 0.06	2.97 ± 0.06	6.1 ± 0.4	5.1 ± 0.2	12 ± 2	51 ± 4	34
$[+24.8^\circ, +44.8^\circ]$	1.26 ± 0.03	3.26 (fixed)	2.6 ± 0.2	3.0 ± 0.2	11 ± 10	5.1 (fixed)	13 ± 4	69 ± 20	53

trend imprinted by the dipole between 4 and 32 EeV; statistical fluctuations dominate above 32 EeV.

Spectral parameters for each declination band, $\mathbf{p}_{\Delta\delta}$, are obtained by applying the combination procedure, except in the northernmost band where only inclined events contribute: they are listed in Table I. A quantitative statement on the statistical agreement between $\mathbf{p}_{\Delta\delta}$ and the reference parameters across $[-84.8^\circ, +24.8^\circ]$, \mathbf{p}_{ref} , can be drawn from the distance-squared quantity

$$Q^2 = (\mathbf{p}_{\Delta\delta} - \mathbf{p}_{\text{ref}})^T (\mathbf{\Sigma}_{\Delta\delta} + \mathbf{\Sigma}_{\text{ref}})^{-1} (\mathbf{p}_{\Delta\delta} - \mathbf{p}_{\text{ref}}), \quad (6)$$

which accounts for the correlations between parameters through their respective covariance matrices $\mathbf{\Sigma}_{\Delta\delta}$ and $\mathbf{\Sigma}_{\text{ref}}$ given in the Appendix A. Some fraction of the uncertainty in the exposure may depend on the declination [27]. The array is slightly tilted by $\simeq 0.2^\circ$ in the southeastern direction $\varphi_{\text{tilt}} \simeq -30^\circ$. Besides, the latitude of the Observatory varies by $\simeq 0.5^\circ$ between detectors located in the northernmost and southernmost positions. Considering the uncertainties in the determination of φ_{tilt} and the impact of the spatial extension of the array, we conservatively allocate an uncertainty of $100 \text{ km}^2 \text{sr yr}$ in the exposure of each declination band that propagates into an additional contribution to the uncertainty in J_0 . The probability that the set of parameters $\mathbf{p}_{\Delta\delta}$ departs from the reference ones is obtained by drawing at random mock samples and by counting the fraction of them displaying a value Q^2 larger than that in data. No significant departure is observed.

Some departure in γ_3 , E_{34} , and γ_4 , which shape the spectrum at the highest energies, are evident in the band $[-51^\circ, -29^\circ]$. The departure remains quasi-identical when fixing the other parameters to their values in the band $[-84.8^\circ, +24.8^\circ]$. This declination range encompasses the Centaurus region in which an overdensity over a circular region of $\simeq 24^\circ$ is present [4] and which has attracted attention in, e.g., Refs. [28–33]. We have estimated the spectral features by restricting further, within the declination band, the region of interest within $\simeq 24^\circ$ around the position (right ascension $\alpha = 201^\circ$, declination $\delta = -43^\circ$) to check whether the harder values of γ_3 and γ_4 as well as

the smaller value of E_{34} elsewhere can be attributed to the overdensity. However, statistical fluctuations prevent drawing any conclusion, given that $\gamma_3 = 2.8 \pm 0.3$, $E_{34} = (67 \pm 11) \text{ EeV}$, and $\gamma_4 = 9 \pm 4$ in that specific region. In parallel, the values obtained by excluding the 24° window around the Centaurus region from the declination band are $\gamma_3 = 2.88 \pm 0.07$, $E_{34} = (37 \pm 4) \text{ EeV}$, and $\gamma_4 = 4.5 \pm 0.5$, close to those observed over the whole $[-51^\circ: -29^\circ]$ band. The same outcome holds about other, more modest, overdensities over the same scale that have attracted attention [30,32,34,35]: $\gamma_3 = 2.9 \pm 0.2$, $E_{34} = (41 \pm 11) \text{ EeV}$, and $\gamma_4 = 5 \pm 1$ around the region of NGC 253 ($\alpha = 11.9^\circ, \delta = -25.3^\circ$), and, within the declination band $[-8^\circ, +24.8^\circ]$, $\gamma_3 = 3.3 \pm 0.3$, $E_{34} = (58 \pm 18) \text{ EeV}$, and $\gamma_4 = 5 \pm 1$ around the region of NGC 1068 galaxy ($\alpha = 40.5^\circ, \delta = 0^\circ$). Finally, since the northernmost declination band is also observed using Telescope Array with an exposure $\simeq 20\%$ larger [36], it is interesting to note that the spectral parameters do not show deviations with respect to those of the $[-84.8^\circ, +24.8^\circ]$ band.

We conclude, consistent with large-scale anisotropy measurements [3] and with our previous report from an exposure of $60,400 \text{ km}^2 \text{sr yr}$ and covering declinations from -90° to $+24.8^\circ$ [7], that the energy spectra are identical to within a mild dipolar modulation with declination from -90° to $+44.8^\circ$.

Spectrum across declinations -90° to $+44.8^\circ$ —Given the statistical agreement of the spectra across declinations, we present in Fig. 3 the combined spectrum across declinations -90° to $+44.8^\circ$, scaled by E^2 (energy flux). The colored band shows the systematic uncertainties, which have been propagated by repeating the analysis on datasets obtained by randomly sampling the different sources of systematics that affect individual energies and exposure. The main contribution stems, by far, from the 14% uncertainty in energy scale. The various spectral features, with their statistical and systematic uncertainties, are given in Fig. 3. The data, included those in each declination band, are listed on a point-by-point basis in the Appendix A.

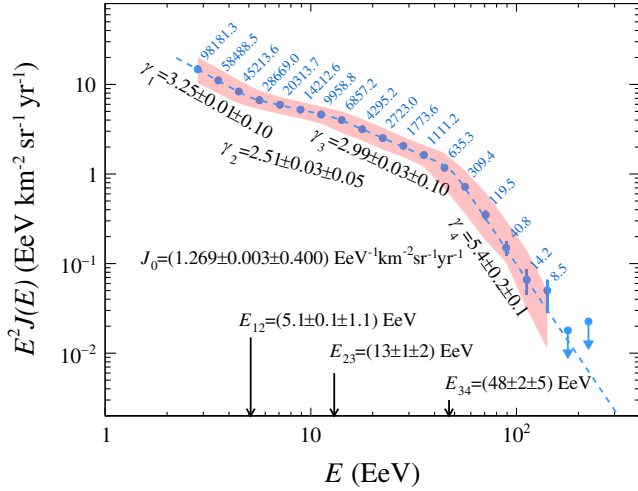


FIG. 3. Energy spectrum scaled by E^2 (energy flux) across declinations $[-90^\circ, +44.8^\circ]$. The number of events corrected for detector effects is indicated in each bin. The red band stands for the systematic uncertainties while the dotted line indicates the best-fit function described by the spectral features given with their statistical and systematic uncertainties. Data are available in the Appendix B.

Beyond the well-known features of the ankle and the steepening, earlier evidence for “instep” [6] is reinforced with this measurement. We had previously disfavored, with 3.9σ confidence, a model of the energy spectrum consisting of a series of two power laws followed by a slow suppression [6]. By drawing at random mock samples of observed energies following this reference model without instep, and by reconstructing the corresponding spectra using the reference model and the alternative one [Eq. (1)], we built the distribution of the test statistics t from the ratio of the likelihood values associated with each hypothesis. Only two out of 10^8 realizations show a test statistic greater than the observed one ($t \approx 38$). Thus for one-sided Gaussian distributions, the reference model can be rejected at the 5.5σ confidence level. The significance remains above 5.5σ when the complete chain of analysis is repeated with the energy scale adjusted by $\pm 14\%$ (the dominant systematic uncertainty) from the nominal one.

Discussion—The first measurement of the energy spectrum of cosmic rays over the entire range of declination covered by the surface array of the Pierre Auger Observatory with an exposure of $104,900 \text{ km}^2 \text{ sr yr}$ has been presented. This is made possible by using independent spectra measured over $[0, 60^\circ]$ and $[60^\circ, 80^\circ]$ combined through a forward-folding procedure that makes use of a unique function to describe the underlying spectrum. Statistical agreement is obtained by increasing the energies inferred from N_{68} values measured between 60° and 80° from $+2.9\%$ at 4 EeV to 3.1% at 10 EeV; the increase then slows and energies are changed by -1% at 100 EeV. Such changes are consistent with the uncertainties in the energy assignments to N_{68} .

A search for a declination dependence was performed by comparing the energy spectrum in five declination ranges with that measured in the band $[-84.8^\circ, +24.8^\circ]$, which is covered when measuring individual spectra between $[0, 60^\circ]$ and $[60^\circ, 80^\circ]$ in zenith angle. All spectra are found to be consistent with the reference one, apart from the mild modulation expected from a dipolar anisotropy previously uncovered [3]. Notably this statement applies to the northernmost declination band $[+24.8^\circ, +44.8^\circ]$, where only inclined events are available.

The combination of the two individual measurements and the statistical agreement across declinations lead to the construction of the spectrum across -90° to $+44.8^\circ$ declinations, where the features of the ankle, the instep and the suppression are firmly established. Among those features, the significance of the instep, originally uncovered with 3.9σ confidence [6], has reached 5.5σ . The increase in significance is consistent with the increase in exposure, in particular from the inclined events.

The absence of declination dependencies disfavors that the origin of the instep feature may be attributed to the distinctive spectrum of a small number of foreground sources contributing significantly to the total intensity. By contrast, the steepening seems to reflect the interplay between the flux contributions of the helium and carbon-nitrogen-oxygen components from rather similar sources [7,37]. This is inline with the narrow range of maximum rigidity at the sources that can be inferred from the succession of rather pure-composition components of nuclei above 10 EeV [38–40]. The improved sensitivity in mass composition with the upgraded observatory [41] will allow further characterization on the instep thus shedding more light on its origin.

Acknowledgments—The successful installation, commissioning, and operation of the Pierre Auger Observatory would not have been possible without the strong commitment and effort from the technical and administrative staff in Malargüe. We are very grateful to the following agencies and organizations for financial support: Argentina—Comisión Nacional de Energía Atómica; Agencia Nacional de Promoción Científica y Tecnológica (ANPCyT); Consejo Nacional de Investigaciones Científicas y Técnicas (CONICET); Gobierno de la Provincia de Mendoza; Municipalidad de Malargüe; NDM Holdings and Valle Las Leñas, in gratitude for their continuing cooperation over land access; Australia—the Australian Research Council; Belgium—Fonds de la Recherche Scientifique (FNRS); Research Foundation Flanders (FWO), Marie Curie Action of the European Union Grant No. 101107047; Brazil—Conselho Nacional de Desenvolvimento Científico e Tecnológico (CNPq); Financiadora de Estudos e Projetos (FINEP); Fundação de Amparo à Pesquisa do Estado de Rio de Janeiro (FAPERJ); São Paulo Research Foundation

(FAPESP) Grants No. 2019/10151-2, No. 2010/07359-6, and No. 1999/05404-3; Ministério da Ciência, Tecnologia, Inovações e Comunicações (MCTIC); Czech Republic—GACR 24-13049S, CAS LQ100102401, MEYS LM2023032, CZ.02.1.01/0.0/0.0/16_013/0001402, CZ.02.1.01/0.0/0.0/18_046/0016010, CZ.02.1.01/0.0/0.0/17_049/0008422, and CZ.02.01.01/00/22_008/0004632; France—Centre de Calcul IN2P3/CNRS; Centre National de la Recherche Scientifique (CNRS); Conseil Régional Ile-de-France; Département Physique Nucléaire et Corpusculaire (PNC-IN2P3/CNRS); Département Sciences de l’Univers (SDU-INSU/CNRS); Institut Lagrange de Paris (ILP) Grant No. LABEX ANR-10-LABX-63 within the Investissements d’Avenir Programme Grant No. ANR-11-IDEX-0004-02; Germany—Bundesministerium für Bildung und Forschung (BMBF); Deutsche Forschungsgemeinschaft (DFG); Finanzministerium Baden-Württemberg; Helmholtz Alliance for Astroparticle Physics (HAP); Helmholtz-Gemeinschaft Deutscher Forschungszentren (HGF); Ministerium für Kultur und Wissenschaft des Landes Nordrhein-Westfalen; Ministerium für Wissenschaft, Forschung und Kunst des Landes Baden-Württemberg; Italy—Istituto Nazionale di Fisica Nucleare (INFN); Istituto Nazionale di Astrofisica (INAF); Ministero dell’Università e della Ricerca (MUR); CETEMPS Center of Excellence; Ministero degli Affari Esteri (MAE), ICSC Centro Nazionale di Ricerca in High Performance Computing, Big Data and Quantum Computing, funded by European Union NextGenerationEU, reference code CN_00000013; México—Consejo Nacional de Ciencia y Tecnología (CONACYT) No. 167733; Universidad Nacional Autónoma de México (UNAM); PAPIIT DGAPA-UNAM; The Netherlands—Ministry of Education, Culture and Science; Netherlands Organisation for Scientific Research (NWO); Dutch national e-infrastructure with the support of SURF Cooperative; Poland—Ministry of Education and Science, Grants No. DIR/WK/2018/11 and No. 2022/WK/12; National Science Centre, Grants No. 2016/22/M/ST9/00198, No. 2016/23/B/ST9/01635, No. 2020/39/B/ST9/01398, and No. 2022/45/B/ST9/02163; Portugal—Portuguese national funds and FEDER funds within Programa Operacional Factores de Competitividade through Fundação para a Ciência e a Tecnologia (COMPETE); Romania—Ministry of Research, Innovation and Digitization, CNCS-UEFISCDI, Contract No. 30N/2023 under Romanian National Core Program LAPLAS VII, Grant No. PN 23 21 01 02 and Project No. PN-III-P1-1.1-TE-2021-0924/TE57/2022, within PNCDI III; Slovenia—Slovenian Research Agency, Grants P1-0031, P1-0385, I0-0033, N1-0111; Spain—Ministerio de Ciencia e Innovación/Agencia Estatal de Investigación (PID2019–105544 GB-I00, PID2022-140510NB-I00, and RYC2019-027017-I), Xunta de Galicia (CIGUS Network of Research Centers, Consolidación 2021 GRC GI-2033, ED431C-2021/22, and

ED431F-2022/15), Junta de Andalucía (SOMM17/6104/UGR and P18-FR-4314), and the European Union (Marie Skłodowska-Curie 101065027 and ERDF); USA—Department of Energy, Contracts No. DE-AC02-07CH11359, No. DE-FR02-04ER41300, No. DE-FG02-99ER41107, and No. DE-SC0011689; National Science Foundation, Grants No. 0450696 and No. NSF-2013199; The Grainger Foundation; Marie Curie-IRSES/EPLANET; European Particle Physics Latin American Network; and UNESCO.

Data availability—The data are not publicly available. The data are available from the authors upon reasonable request.

-
- [1] A. Aab *et al.* (Pierre Auger Collaboration), *Nucl. Instrum. Methods Phys. Res., Sect. A* **798**, 172 (2015).
 - [2] A. Aab *et al.* (Pierre Auger Collaboration), *Science* **357**, 1266 (2017).
 - [3] A. A. Halim *et al.* (Pierre Auger Collaboration), *Astrophys. J.* **976**, 48 (2024).
 - [4] P. Abreu *et al.* (Pierre Auger Collaboration), *Astrophys. J.* **935**, 170 (2022).
 - [5] T. Fujii, *Proc. Sci. ICRC2023 (2024)* 031 [arXiv:2401.08952].
 - [6] A. Aab *et al.* (Pierre Auger Collaboration), *Phys. Rev. D* **102**, 062005 (2020).
 - [7] A. Aab *et al.* (Pierre Auger Collaboration), *Phys. Rev. Lett.* **125**, 121106 (2020).
 - [8] S. Razzaque, *APS Phys.* **13**, 145 (2020).
 - [9] F. Scherb, MIT Nuclear Science Technical Report No. 71, 1959.
 - [10] G. W. Clark, J. Earl, W. L. Kraushaar, J. Linsley, B. B. Rossi, F. Scherb, and D. W. Scott, *Phys. Rev.* **122**, 637 (1961).
 - [11] M. Ave, J. A. Hinton, R. A. Vazquez, A. A. Watson, and E. Zas, *Phys. Rev. Lett.* **85**, 2244 (2000).
 - [12] A. Aab *et al.* (Pierre Auger Collaboration), *J. Instrum.* **15**, P10021 (2020).
 - [13] M. Ave, R. A. Vazquez, and E. Zas, *Astropart. Phys.* **14**, 91 (2000).
 - [14] Pierre Auger Collaboration, *J. Cosmol. Astropart. Phys.* **08** (2014) 019.
 - [15] J. Hersil, I. Escobar, D. Scott, G. Clark, and S. Olbert, *Phys. Rev. Lett.* **6**, 22 (1961).
 - [16] A. Aab *et al.* (Pierre Auger Collaboration), *Phys. Rev. D* **100**, 082003 (2019).
 - [17] Pierre Auger Collaboration, *J. Cosmol. Astropart. Phys.* **08** (2015) 049.
 - [18] H. P. Dembinski, P. Billoir, O. Deligny, and T. Hebbeker, *Astropart. Phys.* **34**, 128 (2010).
 - [19] P. Abreu *et al.* (Pierre Auger Collaboration), *Eur. Phys. J. C* **81**, 966 (2021).
 - [20] V. Verzi *et al.* (Pierre Auger Collaboration), in *Proceedings, 33rd International Cosmic Ray Conference (ICRC2013): Rio de Janeiro, Brazil* (2013), pp. 415–608.
 - [21] J. Abraham *et al.* (Pierre Auger Collaboration), *Nucl. Instrum. Methods Phys. Res., Sect. A* **613**, 29 (2010).

- [22] C. K. Guerard *et al.* (Pierre Auger Collaboration), in *Proceedings of 27th International Cosmic Ray Conference (ICRC 2001)*, 7-15 August 2001. Hamburg, Germany (2002).
- [23] P. Abreu *et al.* (Pierre Auger Collaboration), *Astropart. Phys.* **34**, 368 (2011).
- [24] A. Abdul Halim *et al.* (Pierre Auger Collaboration), *Phys. Rev. Lett.* **134**, 021001 (2025).
- [25] A. Abdul Halim *et al.* (Pierre Auger Collaboration), *Phys. Rev. D* **111**, 022003 (2025).
- [26] M. Bonamente, *J. Appl. Stat.* **47**, 2044 (2020).
- [27] P. Abreu *et al.* (Pierre Auger Collaboration), *Astrophys. J. Suppl. Ser.* **203**, 34 (2012).
- [28] P. L. Biermann and V. de Souza, *Astrophys. J.* **746**, 72 (2012).
- [29] A. Keivani, G. R. Farrar, and M. Sutherland, *Astropart. Phys.* **61**, 47 (2014).
- [30] A. R. Bell and J. H. Matthews, *Mon. Not. R. Astron. Soc.* **511**, 448 (2022).
- [31] S. Mollerach and E. Roulet, *Phys. Rev. D* **110**, 063030 (2024).
- [32] S. Marafico, J. Biteau, A. Condorelli, O. Deligny, and J. Bregeon, *Astrophys. J.* **972**, 4 (2024).
- [33] R. Mbarek, D. Caprioli, and K. Murase, *Phys. Rev. D* **111**, 023024 (2025).
- [34] G. E. Romero, A. L. Müller, and M. Roth, *Astron. Astrophys.* **616**, A57 (2018).
- [35] L. A. Anchordoqui and J. F. Soriano, *Proc. Sci. ICRC2019* (2021) 255 [arXiv:1905.13243].
- [36] R. U. Abbasi *et al.* (Telescope Array Collaboration), arXiv:2406.08612.
- [37] A. A. Halim *et al.* (Pierre Auger Collaboration), *J. Cosmol. Astropart. Phys.* **05** (2023) 024.
- [38] D. Ehlert, F. Oikonomou, and M. Unger, *Phys. Rev. D* **107**, 103045 (2023).
- [39] G. R. Farrar, *Phys. Rev. Lett.* **134**, 081003 (2025).
- [40] B. T. Zhang, K. Murase, N. Ekanger, M. Bhattacharya, and S. Horiuchi, arXiv:2405.17409.
- [41] A. Aab *et al.* (Pierre Auger Collaboration), arXiv:1604.03637.
- [42] B. R. Dawson, L. Valore, R. Colalillo, and F. Guarino (Pierre Auger Collaboration), *EPJ Web Conf.* **197**, 01004 (2019).
- [43] V. M. Harvey *et al.* (Pierre Auger Collaboration), *Proc. Sci. ICRC2023* (2023) 300.
- [44] J. Bellido *et al.* (Pierre Auger Collaboration), *Proc. Sci. ICRC2023* (2023) 211.
- [45] A. Aab *et al.* (Pierre Auger Collaboration), *Phys. Rev. D* **90**, 122005 (2014).
- [46] J. Matthews, *Astropart. Phys.* **22**, 387 (2005).
- [47] T. Pierog, I. Karpenko, J. M. Katzy, E. Yatsenko, and K. Werner, *Phys. Rev. C* **92**, 034906 (2015).
- [48] L. Cazon, R. Conceição, and F. Riehn, *Phys. Lett. B* **784**, 68 (2018).
- [49] C. Bérat, C. Bleve, O. Deligny, F. Montanet, P. Savina, and Z. Torrès, *Astrophys. J.* **929**, 55 (2022).
- [50] C. Berat, A. Condorelli, O. Deligny, F. Montanet, and Z. Torres, *Astrophys. J.* **966**, 186 (2024).

End Matter

Appendix A—Here, we first provide details of the energy-calibration of S_{38} and of N_{68} , and then explain the sources of energy-dependent systematic uncertainties in N_{68} that enter into the budget σ_C and justify the use of a nonzero δC above 10 EeV.

The energy calibration of $S(1000)$ is derived from a two-step process [6]. First, $S(1000)$ is corrected for attenuation effects with zenith angle θ by using the constant intensity cut method [15]. For a given intensity threshold, the attenuation curve is fitted with a third-degree polynomial, $S(1000) = S_{38}(1 + a_S x_S + b_S x_S^2 + c_S x_S^3)$, where $x_S = \cos^2 \theta - \cos^2 38^\circ$ and S_{38} is a zenith-independent shower-size estimator. The intensity-threshold dependence in the curves is accounted for by introducing an empirical dependence in terms of $y_S = \log_{10}(S_{38}/40 \text{ VEM})$ in the coefficients a_S , b_S and c_S through a second-order

TABLE II. Coefficients of the second-degree polynomial in terms of $y_S = \log_{10}(S_{38}/(40 \text{ VEM}))$ for the parameters a_S , b_S , and c_S .

	y_S^0	y_S^1	y_S^2
a_S	0.936	0.005	-0.400
b_S	-1.62	-0.51	-0.13
c_S	-0.92	0.54	1.75

polynomial in y . A VEM corresponds to the energy deposit of one vertical equivalent muon. The polynomial coefficients, updated with respect to those in [6], are given in Table II. They relate to S_{38} values ranging from 15 to 120 VEM. Outside these bounds, the coefficients are set to their values at 15 and 120 VEM. Secondly, the corrected shower-size estimator, S_{38} , is converted into energy E using a power-law calibration relationship, $E = A_S(S_{38})^{B_S}$, determined with high-quality events detected simultaneously with the fluorescence detector. The energy scale is based on [42], with recent improvements concerning aerosol attenuation [43] and longitudinal-profile reconstruction [44]. In this Letter, $A_S = (1.86 \pm 0.03) \times 10^{-1}$ EeV and $B_S = 1.021 \pm 0.004$.

The energy calibration of N_{19} is carried out in the same manner. A constant-intensity-cut correction is applied to the (relative) muon-number estimator N_{19} using a second-degree polynomial, $N_{19} = N_{68}(1 + a_N x_N + b_N x_N^2)$, which is enough to guarantee the same intensity in bins of $\cos^2 \theta$ between 60° and 80° (with $x_N = \cos^2 \theta - \cos^2 68^\circ$). The intensity-threshold dependence is accounted for by introducing an empirical dependence in terms of $y_N = \log_{10}(N_{19})$ in the coefficients a_N and b_N . The polynomial coefficients are given in Table III. They relate to N_{68} values ranging from 0.9 to 4.5. Outside these bounds, the

TABLE III. Coefficients of the first-degree polynomial in terms of $y_N = \log_{10} N_{19}$ for the parameters a_N and b_N .

	y_N^0	y_N^1
a_N	-0.292	0.468
b_N	-4.96	0.79

coefficients are set to their values at 0.9 and 4.5. The energy-calibration relationship is $E = A_N(N_{68})^{B_N}$, with $A_N = (5.29 \pm 0.06)$ EeV and $B_N = 1.046 \pm 0.014$. Note that these values are referred to as $A \pm \sigma_A$ and $B \pm \sigma_B$ in the main text.

Since N_{68} depends on the mass composition of the primary particles, its calibration relationship to the energy measured with the fluorescence technique accounts for the trend of the composition change with energy inherently as the underlying mass distribution is directly sampled by the fluorescence detectors. The use of a single power law for the relationship between N_{68} and E is then justified only for a single logarithmic evolution of the composition as a function of energy. This turns out to be the case, within the statistical uncertainties of the fluorescence dataset, above $\simeq 2$ EeV [45]. However, using deep-neural-network techniques applied to the surface-detector dataset, sharp changes of the elongation rate, too small to show up within the statistics available with the fluorescence technique, have recently been uncovered around $\simeq 6$ EeV, $\simeq 10$ EeV, and $\simeq 30$ EeV [24,25]. The impact of these elongation rate changes on the energy calibration of N_{68} can be estimated as follows. Within the Heitler-Matthews superposition model of air shower [46], the number of muons N_μ increases with the cosmic-ray mass number A as $N_\mu \propto A^{1-\beta}$. Assuming that the slope of N_{68} with A follows that of N_μ , the change of slope of N_{68} , $\Delta m_{N_{68}}$, can be related to that of the shower maximum slant depth, $\Delta m_{X_{\max}}$ through

$$\Delta m_{N_{68}} = -\frac{1-\beta}{D_0} \Delta m_{X_{\max}}, \quad (\text{A1})$$

with $D_0 \simeq 56.1$ g cm $^{-2}$ the elongate rate of protons expected from EPOS-LHC [47]. Using $\beta \simeq 0.927$ as a benchmark [48], and considering to first order a single change of elongation rate around 10 EeV to describe the observed series of kinks from below 6 EeV to above 30 EeV, we get an amplitude for the expected nonlinearity of N_{68} of $\simeq 2.5\%$ per decade. We note that we neglect here the correlated nonlinearity effects in the energy calibration of S_{38} as they are smaller.

Another source of logarithmic nonlinearities between N_{68} and E stems from the use of the constant-intensity-cut correction to make uniform the distribution of events in terms of $\sin^2 \theta$. The correction is necessary to compensate for imperfections of the N_{19} energy estimator, which accounts for muon contributions to the signals and requires

model-dependent corrections for electromagnetic ones, not negligible between $\theta = 60^\circ$ and $\theta \simeq 70^\circ$. However, smaller, yet genuine, deviations of the $\sin^2 \theta$ distribution from uniformity, Δ , are expected in presence of dipolar anisotropies. They can be estimated as [27]

$$\Delta = \frac{N_{\text{dip}}}{N_{\text{iso}}} d_z \sin \lambda \cos \theta, \quad (\text{A2})$$

with N_{iso} (N_{dip}) the expected number of events in the covered region of the sky for an isotropic (a dipolar) angular distribution. While Δ is well within 1% for $\theta \leq 60^\circ$ for the dipole components d_z of interest (measured with large uncertainties, though), it increases up to, on average, $\simeq 3\%$ for $\theta \geq 60^\circ$. We estimated that the uniformity of the $\sin^2 \theta$ distribution forced by the constant intensity correction for $N_{68} < 4.5$ ($E \simeq 20$ EeV) can then lead to energy distortions of $\simeq 1.5\%$ between 4 and $\simeq 20$ EeV, while higher energies would not be impacted as the energy dependence of the polynomial coefficients relating N_{19} to N_{68} is frozen. This effectively acts as a source of non-linearity that occurs around $\simeq 20$ EeV.

Overall, we add in quadrature both sources of non-linearities and end up with $\sigma_C = 3 \times 10^{-2}$, and choose, as a first-order approximation, the transition energy at 10 EeV. We have checked that the best-fit value for δC is mildly impacted when increasing σ_C to 5×10^{-2} or increasing the transition energy.

Appendix B—Here, we provide a few summary plots and data related to the analysis presented in the main Letter.

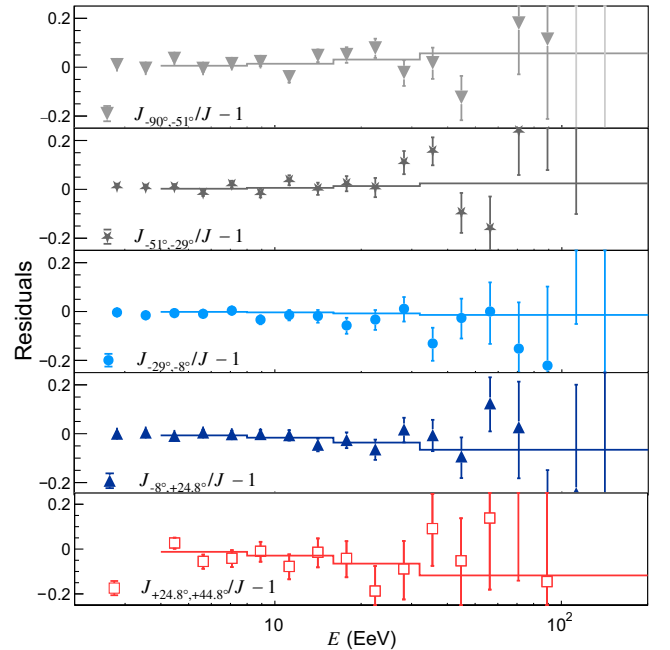

 FIG. 4. Energy-spectra residuals enlarged within $\pm 25\%$ in the five declination bands.

TABLE IV. Correlation matrix relative to Σ_{ref} expressed in a basis $(J_0, \gamma_1, E_{12}, \gamma_2, E_{23}, \gamma_3, E_{34}, \gamma_4)$.

+1.000	-0.535	+0.613	-0.396	-0.162	+0.218	-0.182	-0.317
	+1.000	-0.782	+0.494	+0.343	+0.111	+0.561	+0.512
		+1.000	-0.872	-0.609	-0.186	-0.329	-0.303
			+1.000	+0.827	+0.313	+0.104	+0.052
				+1.000	+0.594	+0.007	-0.052
					+1.000	+0.133	-0.186
						+1.000	+0.431
							+1.000

The response function for events between 0 and 60° is described in detail in our previous paper [6]. We have applied the same data-driven techniques to determine that for events between 60° and 80° . The resolution function is parameterized as a Gaussian function with σ_N parameter evolving with energy as

$$\frac{\sigma_N(E)}{E} = 0.046 + \frac{0.34}{\sqrt{E}}, \quad (\text{B1})$$

with E in EeV. No significant bias is found in the sub-threshold energy bins of interest, down to 2.5 EeV. The efficiency is described as (still with E in EeV)

$$\varepsilon(E) = 0.5 \left(1 + \operatorname{erf} \left(\frac{\log_{10} E}{0.34} \right) \right). \quad (\text{B2})$$

In Fig. 4, we present an alternative version of the bottom panel of Fig. 2. Here, the energy-spectra residuals in the five declination bands are enlarged within $\pm 25\%$ while no artificial shifts are applied for visualization purpose; some data points at high energies therefore lie outside the windows. The reference lines are the best-fit function for the spectrum combined over $[-84.8^\circ, +24.8^\circ]$ accounting for dipole anisotropies.

The correlation matrix relative to the covariance matrices used to search for differences in the spectral features is given in Table IV. It provides, together with the corresponding uncertainties in the parameters listed in Table I, the coefficients needed to get Σ_{ref} as well as $\Sigma_{\Delta\delta}$.

The combined spectrum data points with their statistical and systematic uncertainties are collected in Table V together with the observed and corrected number of events, while the correlation matrix of the spectrum data points that accounts for systematic uncertainties is given in Table VI. The strong bin-to-bin correlations observed stem from systematic uncertainties dominated by those in the energy scale: for a single power-law spectrum in $E^{-\gamma}$, a $\Delta E/E$

TABLE V. Combined spectrum data.

\log_{10} (E/EeV)	$J(E) \pm \sigma_{\text{stat}}(E) \pm \sigma_{\text{syst}}(E)$ ($\text{EeV}^{-1} \text{ km}^{-2} \text{ sr}^{-1} \text{ yr}^{-1}$)	n	n_{corr}
0.45	$(1.8614^{+0.0065+0.7}_{-0.0065-0.6}) \times 10^0$	107,232	98178.2
0.55	$(8.808^{+0.040+3.2}_{-0.040-2.5}) \times 10^{-1}$	61,873	58483.8
0.65	$(4.183^{+0.022+1.4}_{-0.022-1.1}) \times 10^{-1}$	48,929	45207.8
0.75	$(2.107^{+0.014+0.6}_{-0.014-0.4}) \times 10^{-1}$	30,525	28678.2
0.85	$(1.186^{+0.009+0.3}_{-0.009-0.3}) \times 10^{-1}$	20,984	20314.9
0.95	$(6.590^{+0.059+1.5}_{-0.059-1.4}) \times 10^{-2}$	14,590	14213.9
1.05	$(3.668^{+0.039+0.9}_{-0.039-0.8}) \times 10^{-2}$	10,159	9957.9
1.15	$(2.001^{+0.024+0.5}_{-0.026-0.6}) \times 10^{-2}$	6984	6858.1
1.25	$(9.982^{+0.152+3.0}_{-0.165-2.8}) \times 10^{-3}$	4396	4296.4
1.35	$(5.027^{+0.097+1.5}_{-0.101-1.3}) \times 10^{-3}$	2775	2724.0
1.45	$(2.600^{+0.062+0.7}_{-0.067-0.7}) \times 10^{-3}$	1800	1773.7
1.55	$(1.294^{+0.039+0.4}_{-0.043-0.3}) \times 10^{-3}$	1124	1112.3
1.65	$(5.88^{+0.23+2.7}_{-0.26-2.4}) \times 10^{-4}$	634	635.3
1.75	$(2.27^{+0.13+1.2}_{-0.14-1.1}) \times 10^{-4}$	318	309.3
1.85	$(6.98^{+0.67+5.3}_{-0.69-3.4}) \times 10^{-5}$	126	119.5
1.95	$(1.89^{+0.29+1.9}_{-0.32-0.6}) \times 10^{-5}$	43	40.8
2.05	$(5.3^{+1.4+6.0}_{-1.6-2.8}) \times 10^{-6}$	15	14.2
2.15	$(2.5^{+0.7+0.1}_{-1.1-1.9}) \times 10^{-6}$	9	8.5
2.25	$< 5.4 \times 10^{-7}$	0	0
2.35	$< 4.3 \times 10^{-7}$	0	0

TABLE VI. Correlation matrix of the spectrum accounting for systematic uncertainties.

i	j																	
	0.45	0.55	0.65	0.75	0.85	0.95	1.05	1.15	1.25	1.35	1.45	1.55	1.65	1.75	1.85	1.95	2.05	2.15
0.45	1	0.984	0.983	0.980	0.985	0.991	0.986	0.976	0.971	0.970	0.980	0.987	0.990	0.983	0.974	0.946	0.957	0.788
0.55		1	0.999	0.999	0.993	0.993	0.986	0.977	0.978	0.977	0.981	0.986	0.990	0.997	0.994	0.973	0.963	0.848
0.65			1	0.999	0.994	0.993	0.984	0.975	0.977	0.975	0.983	0.987	0.991	0.997	0.994	0.972	0.962	0.853
0.75				1	0.993	0.991	0.982	0.970	0.971	0.970	0.978	0.987	0.989	0.997	0.994	0.974	0.960	0.851
0.85					1	0.997	0.986	0.977	0.967	0.965	0.986	0.996	0.997	0.992	0.982	0.949	0.955	0.859
0.95						1	0.992	0.985	0.977	0.974	0.986	0.994	0.994	0.990	0.981	0.953	0.951	0.842
1.05							1	0.994	0.991	0.989	0.980	0.985	0.982	0.976	0.971	0.945	0.949	0.805
1.15								1	0.993	0.992	0.981	0.973	0.974	0.964	0.958	0.924	0.941	0.813
1.25									1	0.998	0.976	0.964	0.963	0.964	0.965	0.943	0.937	0.803
1.35										1	0.973	0.961	0.963	0.962	0.962	0.942	0.943	0.787
1.45											1	0.986	0.984	0.974	0.963	0.922	0.941	0.850
1.55												1	0.993	0.983	0.974	0.937	0.944	0.842
1.65													1	0.989	0.978	0.946	0.962	0.832
1.75														1	0.994	0.974	0.959	0.852
1.85															1	0.981	0.949	0.849
1.95																1	0.923	0.785
2.05																	1	0.756
2.15																		1

 TABLE VII. Spectrum data over the declination band $[-90^\circ, -51^\circ]$.

\log_{10} (E/EeV)	$J(E) \pm \sigma_{\text{stat}}(E)$ ($\text{EeV}^{-1} \text{ km}^{-2} \text{ sr}^{-1} \text{ yr}^{-1}$)	n	n_{corr}
0.45	$(1.875^{+0.013}_{-0.013}) \times 10^0$	24,889	22728.5
0.55	$(8.797^{+0.082}_{-0.081}) \times 10^{-1}$	14,198	13424.9
0.65	$(4.294^{+0.041}_{-0.045}) \times 10^{-1}$	11,557	10693.2
0.75	$(2.114^{+0.026}_{-0.028}) \times 10^{-1}$	7045	6628.6
0.85	$(1.194^{+0.017}_{-0.019}) \times 10^{-1}$	4873	4714.3
0.95	$(6.793^{+0.116}_{-0.126}) \times 10^{-2}$	3470	3375.1
1.05	$(3.549^{+0.075}_{-0.082}) \times 10^{-2}$	2278	2220.4
1.15	$(2.104^{+0.052}_{-0.057}) \times 10^{-2}$	1685	1657.4
1.25	$(1.057^{+0.032}_{-0.035}) \times 10^{-2}$	1057	1048.1

(Table continued)

TABLE VII. (Continued)

\log_{10} (E/EeV)	$J(E) \pm \sigma_{\text{stat}}(E)$ ($\text{EeV}^{-1} \text{ km}^{-2} \text{ sr}^{-1} \text{ yr}^{-1}$)	n	n_{corr}
1.35	$(5.49^{+0.21}_{-0.22}) \times 10^{-3}$	699	684.7
1.45	$(2.48^{+0.13}_{-0.14}) \times 10^{-3}$	397	389.4
1.55	$(1.30^{+0.08}_{-0.09}) \times 10^{-3}$	263	258.0
1.65	$(5.54^{+0.49}_{-0.52}) \times 10^{-4}$	141	137.9
1.75	$(2.78^{+0.30}_{-0.31}) \times 10^{-4}$	85	86.8
1.85	$(7.7^{+1.4}_{-1.6}) \times 10^{-5}$	31	30.3
1.95	$(2.1^{+0.7}_{-0.7}) \times 10^{-5}$	12	10.4
2.05	$(1.4^{+1.8}_{-1.2}) \times 10^{-6}$	1	0.9
2.15	$(1.1^{+1.4}_{-0.9}) \times 10^{-6}$	1	0.9
2.25	$< 2.0 \times 10^{-6}$	0	0
2.35	$< 1.6 \times 10^{-6}$	0	0

TABLE VIII. Spectrum data over the declination band $[-51^\circ, -29^\circ]$.

\log_{10} (E/EeV)	$J(E) \pm \sigma_{\text{stat}}(E)$ (EeV $^{-1}$ km $^{-2}$ sr $^{-1}$ yr $^{-1}$)	n	n_{corr}
0.45	$(1.881_{-0.012}^{+0.012}) \times 10^0$	29,491	27226.2
0.55	$(8.921_{-0.076}^{+0.076}) \times 10^{-1}$	17,193	16258.8
0.65	$(4.192_{-0.043}^{+0.039}) \times 10^{-1}$	12,052	11194.9
0.75	$(2.095_{-0.027}^{+0.025}) \times 10^{-1}$	7509	7044.0
0.85	$(1.202_{-0.019}^{+0.017}) \times 10^{-1}$	5247	5088.8
0.95	$(6.544_{-0.119}^{+0.110}) \times 10^{-2}$	3565	3487.2
1.05	$(3.836_{-0.082}^{+0.075}) \times 10^{-2}$	2616	2573.7
1.15	$(2.015_{-0.052}^{+0.048}) \times 10^{-2}$	1743	1702.3
1.25	$(1.030_{-0.033}^{+0.031}) \times 10^{-2}$	1118	1095.3
1.35	$(5.13_{-0.21}^{+0.20}) \times 10^{-3}$	697	686.8
1.45	$(2.82_{-0.14}^{+0.13}) \times 10^{-3}$	479	474.8
1.55	$(1.48_{-0.09}^{+0.08}) \times 10^{-3}$	313	314.9
1.65	$(5.72_{-0.48}^{+0.46}) \times 10^{-4}$	157	152.9
1.75	$(1.84_{-0.24}^{+0.24}) \times 10^{-4}$	65	62.0
1.85	$(8.1_{-1.5}^{+1.4}) \times 10^{-5}$	35	34.2
1.95	$(2.7_{-0.7}^{+0.8}) \times 10^{-5}$	15	14.7
2.05	$(7.3_{-2.8}^{+3.2}) \times 10^{-6}$	5	4.9
2.15	$(5.8_{-2.3}^{+2.5}) \times 10^{-6}$	5	4.9
2.25	$< 2.1 \times 10^{-6}$	0	0
2.35	$< 1.7 \times 10^{-6}$	0	0

 TABLE IX. Spectrum data over the declination band $[-29^\circ, -8^\circ]$.

\log_{10} (E/EeV)	$J(E) \pm \sigma_{\text{stat}}(E)$ (EeV $^{-1}$ km $^{-2}$ sr $^{-1}$ yr $^{-1}$)	n	n_{corr}
0.45	$(1.850_{-0.012}^{+0.012}) \times 10^{-0}$	28,269	25961.0
0.55	$(8.703_{-0.076}^{+0.076}) \times 10^{-1}$	16,303	15376.7
0.65	$(4.119_{-0.043}^{+0.039}) \times 10^{-1}$	11,529	10677.9
0.75	$(2.105_{-0.027}^{+0.025}) \times 10^{-1}$	7258	6870.6
0.85	$(1.182_{-0.018}^{+0.017}) \times 10^{-1}$	5003	4854.1
0.95	$(6.420_{-0.119}^{+0.111}) \times 10^{-2}$	3408	3319.7
1.05	$(3.642_{-0.080}^{+0.075}) \times 10^{-2}$	2420	2371.2
1.15	$(1.972_{-0.054}^{+0.049}) \times 10^{-2}$	1646	1615.9
1.25	$(9.482_{-0.323}^{+0.296}) \times 10^{-3}$	1001	978.3
1.35	$(4.92_{-0.21}^{+0.19}) \times 10^{-3}$	651	639.1
1.45	$(2.56_{-0.14}^{+0.13}) \times 10^{-3}$	425	419.0
1.55	$(1.11_{-0.08}^{+0.07}) \times 10^{-3}$	232	229.3
1.65	$(6.15_{-0.52}^{+0.49}) \times 10^{-4}$	159	159.4
1.75	$(2.19_{-0.29}^{+0.26}) \times 10^{-4}$	73	71.5
1.85	$(5.5_{-1.1}^{+1.0}) \times 10^{-5}$	24	22.7
1.95	$(1.5_{-0.5}^{+0.5}) \times 10^{-5}$	8	7.5
2.05	$(8.7_{-4.1}^{+3.6}) \times 10^{-6}$	6	5.7
2.15	$(1.2_{-1.0}^{+1.3}) \times 10^{-6}$	1	0.9
2.25	$< 2.2 \times 10^{-6}$	0	0
2.35	$< 1.7 \times 10^{-6}$	0	0

TABLE X. Spectrum data over the declination band $[-8^\circ, +24.8^\circ]$.

\log_{10} (E/EeV)	$J(E) \pm \sigma_{\text{stat}}(E)$ (EeV $^{-1}$ km $^{-2}$ sr $^{-1}$ yr $^{-1}$)	n	n_{corr}
0.45	$(1.857^{+0.013}_{-0.013}) \times 10^0$	24,477	22123.1
0.55	$(8.880^{+0.083}_{-0.083}) \times 10^{-1}$	14,109	13320.9
0.65	$(4.109^{+0.039}_{-0.043}) \times 10^{-1}$	11,712	10776.8
0.75	$(2.136^{+0.025}_{-0.028}) \times 10^{-1}$	7523	7055.6
0.85	$(1.175^{+0.017}_{-0.018}) \times 10^{-1}$	5048	4885.2
0.95	$(6.632^{+0.111}_{-0.122}) \times 10^{-2}$	3560	3471.6
1.05	$(3.673^{+0.074}_{-0.080}) \times 10^{-2}$	2464	2420.3
1.15	$(1.918^{+0.048}_{-0.053}) \times 10^{-2}$	1634	1591.4
1.25	$(9.796^{+0.305}_{-0.327}) \times 10^{-3}$	1049	1023.0
1.35	$(4.76^{+0.19}_{-0.21}) \times 10^{-3}$	638	625.9
1.45	$(2.57^{+0.12}_{-0.14}) \times 10^{-3}$	433	426.6
1.55	$(1.27^{+0.07}_{-0.08}) \times 10^{-3}$	269	265.4
1.65	$(5.72^{+0.45}_{-0.51}) \times 10^{-4}$	150	150.2
1.75	$(2.46^{+0.26}_{-0.28}) \times 10^{-4}$	82	81.4
1.85	$(6.7^{+1.3}_{-1.4}) \times 10^{-5}$	30	27.8
1.95	$(1.0^{+0.5}_{-0.5}) \times 10^{-5}$	6	5.5
2.05	$(4.2^{+1.9}_{-2.7}) \times 10^{-6}$	3	2.8
2.15	$(2.2^{+1.4}_{-2.1}) \times 10^{-6}$	2	1.8
2.25	$< 2.0 \times 10^{-6}$	0	0
2.35	$< 1.6 \times 10^{-6}$	0	0

change in energy scale translates indeed as a change $\Delta J(E)/J(E) = (\gamma - 1)\Delta E/E$. The correlation matrix together with the uncertainties collected in Table V allow for a direct model/data comparison through a generalized

 TABLE XI. Spectrum data over the declination band $[+24.8^\circ, +44.8^\circ]$.

\log_{10} (E/EeV)	$J(E) \pm \sigma_{\text{stat}}(E)$ (EeV $^{-1}$ km $^{-2}$ sr $^{-1}$ yr $^{-1}$)	n	n_{corr}
0.65	$(4.259^{+0.100}_{-0.109}) \times 10^{-1}$	2037	1793.8
0.75	$(2.008^{+0.061}_{-0.066}) \times 10^{-1}$	1172	1064.9
0.85	$(1.13^{+0.04}_{-0.04}) \times 10^{-1}$	793	753.6
0.95	$(6.58^{+0.28}_{-0.31}) \times 10^{-2}$	574	552.7
1.05	$(3.41^{+0.18}_{-0.19}) \times 10^{-2}$	371	360.6
1.15	$(1.98^{+0.13}_{-0.13}) \times 10^{-2}$	270	263.7
1.25	$(9.63^{+0.74}_{-0.81}) \times 10^{-3}$	167	161.6
1.35	$(4.13^{+0.46}_{-0.49}) \times 10^{-3}$	90	87.3
1.45	$(2.31^{+0.29}_{-0.31}) \times 10^{-3}$	63	61.4
1.55	$(1.4^{+0.2}_{-0.2}) \times 10^{-3}$	48	46.8
1.65	$(6.0^{+1.1}_{-1.2}) \times 10^{-4}$	26	25.2
1.75	$(2.5^{+0.75}_{-0.8}) \times 10^{-4}$	13	13.2
1.85	$(9.1^{+4.3}_{-4.6}) \times 10^{-5}$	6	6.1
1.95	$(1.6^{+0.8}_{-1.4}) \times 10^{-5}$	2	1.3
2.05	$< 1.2 \times 10^{-5}$	0	0
2.15	$< 9.8 \times 10^{-6}$	0	0
2.25	$< 8.0 \times 10^{-6}$	0	0
2.35	$< 6.5 \times 10^{-6}$	0	0

χ^2 that accounts for all sources of uncertainties. It can also be used to propagate uncertainties in any quantity derived from the cosmic-ray spectrum, such as cosmogenic gamma-ray [49] or neutrino fluxes [50].

Finally, the spectra obtained in each declination band are collected in Tables VII–XI.